

How do the liquid properties affect the entrapment of bubbles in gas sheared liquid flows?

Avick Sinha^a, Andrey Cherdantsev^b, Kathy Johnson^{a,*}, Joao Vasques^{a,c}, David Hann^{a,b}

^a*Gas Turbine and Transmissions Research Centre (G2TRC), University of Nottingham, Nottingham NG7 2RD, UK.*

^b*Laurentiev Institute of Hydrodynamics, Novosibirsk, Russia*

^c*DNV GL Industrial Services, Loughborough, UK (current)*

Abstract

A large number of industries use fossil fuels for the purpose of cooling and lubrication utilizing a gas stream that acts as a shearing force on the liquid surface. Decreasing the carbon footprint of these processes needs an improved understanding of the effect of liquid properties. To this end this study investigates experimentally the effect of varying surface tension and liquid viscosity on the bubble generation and film statistics in a gas-sheared liquid flow. The experiments were conducted in a horizontal rectangular channel using high speed imaging in conjunction with the Brightness-Based Laser-induced Fluorescence technique (BBLIF) to measure film thickness over an area with a spatial resolution of 40 μm and a temporal resolution of 10kHz. Two butanol-water solutions were used to give reduced surface tensions (namely 0.049 N/m and 0.04 N/m) compared to our previously-studied water only value. Also, two glycerol-water solutions were chosen to yield surface tension values closer to those of an oil of interest (namely 1.4 cP and 1.9 cP).

The results show that compared to water, an increase in film thickness and a decrease in the disturbance wave velocity was observed with either the reduction in the surface tension or increase in the liquid viscosity. The frequency and size of the waves were found to be dominated by the liquid surface tension. Moreover, surface tension was found to have more of an effect on aeration as compared to viscosity. The bubble velocity was found to decrease with increase in viscosity, while it increases with decrease in surface tension. It is suggested that these changes would affect heat transfer and hence should be studied in more detail.

Keywords: Gas-sheared liquid film, Surface tension, Viscosity, Aeration, Film thickness.

1. Introduction

The increase in global warming over the years, has meant that it is an imperative that engineers work to decrease the carbon footprint of industrial processes and transportation. Many of these processes involve the interaction of a liquid layer for cooling or lubrication, with a gas stream that acts as shearing force on the surface. This can produce misting where liquid is embedded in the gas and foaming where gas is embedded in the liquid. This mixing of phases can affect the flow dynamics, in either a beneficial

*Corresponding author

Email address: Kathy.Johnson@nottingham.ac.uk (Kathy Johnson)

or detrimental way. For example foaming can decrease heat transfer from the wall to the liquid, while misting can enhance heat transfer from the liquid to the gas core.

Being able to simulate this process will allow the optimisation of systems. However in order for these models to be trustworthy, the mechanisms need to be validated by fundamental experimentation. This is needed because this flow configuration is complex with much still to understand about the interactions. The analysis supporting the fundamental work presented here was partially undertaken in the COAST project and forms part of a campaign to understand these processes and to provide validation results for complementary CFD work carried out in G2TRC. However, the work has wide applicability as multiphase flow in a channel/pipe occurs in a variety of industrial equipment and processes, such as in heat exchangers, steam generators and evaporators [1]. Understanding the physics behind such flows is important for many applications such as nuclear reactor safety analysis [2], flow assurance in oil and gas [3] and inside the bearing chambers in aero-engines [4].

In such flows, typically the rate of heat and mass transfer is massive due to rapid turbulent mixing and augmentation in the interfacial area. Misting and foaming increase the interfacial surface area and the surface of the film can be covered with complex wavy structures. These structures known as disturbance waves can form at high gas and liquid flow rates. Disturbance waves travel at a high velocity over a significant distance on the top of the residual liquid, which is called the base film [5]. Small scale structures in the form of ripples, can coexist with the disturbance waves. The ripples can travel on the disturbance waves or over the base film. At high gas and liquid flow rates, droplets are ripped from the liquid surface via formation and destruction of transitional structures such as liquid bags and ligaments; subsequently, they get entrained into the gas stream. Cherdantsev et al. [6] observed that, when the entrained droplet in the gas core impinges on the liquid film, it may create a long and a narrow furrow on the film surface. The protruding droplet generates a strong shear due to Kelvin-Helmholtz (K-H) instability. This causes the film surface to be engulfed with short transversely-oriented waves.

The most intriguing phenomenon during droplet/ligament impact is the enormous entrapment of gas bubbles behind the penetrating droplet [7]. The presence of bubbles in a gas-sheared flow has been reported in various experimental studies [1, 7, 8]. Gas bubbles inside a liquid film play a significant role in altering the flow dynamics and the presence of a large number of bubbles can change the overall hydrodynamic properties of the liquid film such as viscosity and density [7]. Bubbles can also increase the interfacial area; hence, between the duct wall and the entrapped bubble, the film becomes much thinner. This can increase the local heat transfer processes [9]. The bubbles can act as nucleation sites for boiling (if bubbles are stuck to the duct wall) and can initiate the nucleate boiling process. Barbosa et al. [10] observed the initiation of nucleate boiling due to the passing of disturbance waves in which a large amount of bubbles were entrapped.

To date, very little attention has been paid to the effects of surface tension and viscosity on the bubble spectra. This is important for thermal applications where surface tension and viscosity can change significantly with temperature. Thus, it is essential to investigate the effects of viscosity and surface tension on bubble generation. Only three papers have been found investigating the bubble dynamics in gas-sheared/annular flows with water as the working fluid. Rodriguez and Shedd [8] used a

backlit visualisation technique to study the bubble count and bubble sizes in a horizontal duct with a high spatial resolution ($4.2 \mu\text{m}/\text{pixel}$). However, they conducted the measurements only at low frequency and inside the base film. This will bias the bubble sizes as larger bubbles are present inside the disturbance waves. Hann et al. [7] carried out investigation of the entrapped bubbles in a horizontal channel using the brightness-based laser-induced fluorescence technique (BBLIF) at high frequency (10 kHz). In their work, they gave a detailed understanding of the bubble evolution from entrapment to collapse. Both these papers showed that the bubble count increases with an increase in gas velocity and liquid Reynolds number. The third paper, by Zadrazil et al. [11], measured the bubble frequency and its spectra along with statistical characteristics of the waves using the Planar Laser-Induced Fluorescence Technique (PLIF). They assumed that the entrapment of bubbles is due to the presence of large-amplitude waves.

Rich literature is available on the effect of viscosity and surface tension on the film thickness. Sadatomi et al. [12] conducted gas-liquid sheared flow experiments on pipes of different diameter using a photographic technique. From their experiments, it was observed that there is a noticeable difference in the film thickness at their lowest surface tension considered (14 mN.m^{-1}) as compared to a water-gas case at the same gas velocity and liquid Reynolds number. The effect of higher surface tension (28 mN.m^{-1} and 42 mN.m^{-1}) on the film thickness was found to be weak. A decrease in film thickness with decrease in surface tension was also observed by Rivera et al. [13], in a vertical annular flow using a conductance probe for various liquid surface tensions. Fukano & Furukawa [14] also used a conductance probe to investigate the effect of viscosity on film thickness. They observed that the film thickness increases with an increase in liquid viscosity. A similar observation was also made by Yoshinaga et al. [15].

Most of the past experiments were carried out by direct high-speed imaging or by employing a conductance probe. The disadvantage of the high-speed imaging is that it cannot provide high accuracy quantitative information unless the camera is orthogonal to the flow and the images calibrated, while the downside of using the conductance probe is its low resolution, and also the results from such probes are affected when the bubble concentration is high. Thus, a non-intrusive optical-based technique is best suited for such complex multi-phase flows. They not only provide high temporal and spatial resolution, but they are also have a minimal effect on the flow dynamics. In the present study, the brightness-based laser-induced fluorescence (BBLIF) technique was used as it most suitable for such flows. Recently, Alekseenko et al. [16] showed that the BBLIF technique could measure not only the film thickness but also the droplet and bubble spectra. Thus, this technique allows simultaneous investigation of the film thickness and 3D film structure along with the entrapped bubbles, which can help in better comprehension of the flow dynamics.

The present work investigates the effect of viscosity and surface tension on the bubble spectra, wave and film statistics as this insight is important for various engineering and science applications including those mentioned above. Previously Vasques et al. [4] have observed that reducing liquid surface tension will increase the bubble count. This work extends knowledge in this important field by further investigating the effect of surface tension on film aeration and film statistics, and also a comparison of the above parameters with varying fluid viscosity.

The paper is structured as follows: the experimental set-up and measurement technique are explained

in Section 2. Section 3 provides a brief description of the bubble tracking algorithm and its effectiveness. The results obtained are categorized in Sections 4 and 5. In Section 4, we discuss wave and film statistics and in Section 5, we discuss bubble dynamics. Section 6 briefly describes how the liquid properties will affect the heat transfer phenomenon in such multi-phase flows. The final section provides the key messages and summarizes the present work.

2. Experimental setup and technique

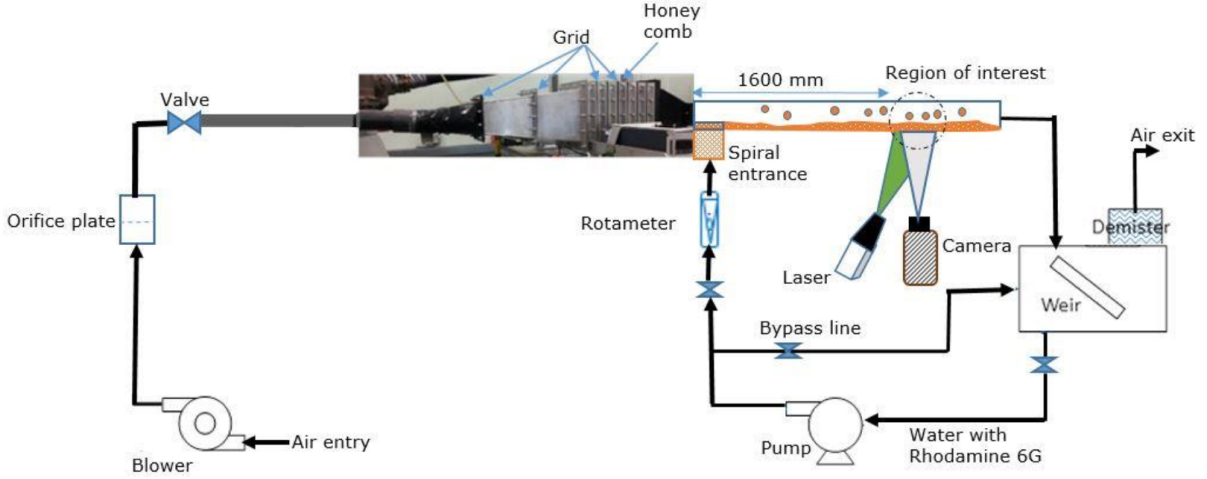


Figure 1: Schematic diagram of the experimental set-up used in the present study using BBLIF technique. Measurements were carried out 1600 mm from the inlet.

Figure 1 shows a schematic diagram of the shearing rig, which is used in the present study. The same rig was used by Hann et al. [7] and Cherdantsev et al. [6] to investigate bubble/droplet formation in gas-sheared liquid films. It consists of a horizontal transparent rectangular duct (material - perspex and glass) with dimensions of 2000 mm \times 166 mm \times 25 mm in length, width, and height, respectively. This gives the hydraulic diameter, D_h , of the duct as 43 mm. A blower (15 kW) is used to supply the air inside the test section, while the liquid was pumped continuously into the rig through the base of the rectangular chamber. To straighten the airflow, a honeycomb grid was placed before the test entrance section. The airflow rate was controlled by monitoring the pressure drop across an orifice plate, and it was calibrated using a pitot tube in a dry duct. The accuracy of the orifice meter reading is \approx 1% of reading. The liquid flow rate was measured using a float rotameter (MPB Industries LTD, UK) and it was also calibrated for the various liquids used in the present study. The range of the rotameter is up to 10 l/min, with an accuracy of 10% of reading. Ball valves were used for control of the liquid flow rate. The inlet of the channel was divided into two by a horizontal plate located 3 mm above the duct bottom. Air was introduced above the horizontal plate, while the liquid entered into the channel below the horizontal plate. The liquid was sheared by the gas flow along the entire test section. Thermocouples were used to measure the instantaneous air and liquid temperature. It was observed that the temperatures for both air (35-40 $^{\circ}$ C) and liquid (18-21 $^{\circ}$ C) were stable during the runs. The temperature of the gas-phase is higher as compared to the liquid phase due to the effect of the blower.

To investigate the effect of surface tension and viscosity, two butanol-water (B–W), and two glycerol-water (G–W) solutions were used in the present study. Butanol was added to the water to give reduced surface tensions of 0.049 N/m (1.5% butanol) and 0.040 N/m (2.5% butanol) as compared to pure water with 0.072 N/m. Glycerol was added to the water to increase the viscosity of the liquid, yielding properties closer to those of certain types of oil of interest. Dynamic viscosities of 0.0014 N/ms (12% Glycerol) and 0.0019 N/ms (20% Glycerol) were obtained in the present study. The properties of the solutions are given in Table 1. The density, surface tension, and viscosity of each solution were calculated using a densitometer, pendant drop method, and Ostwald viscometer, respectively at temperature representing the liquid temperature. The above parameters were measured three times for confidence.

Table 1: Physical properties of the various liquids used in the present study

Property	1.5% B-W	2.5% B-W	12% G-W	20% G-W
Density (ρ , kg/m^3)	994 \pm 2	993 \pm 3	1032 \pm 3	1056 \pm 5
Viscosity (μ , cP)	1.06 \pm 0.11	1.07 \pm 0.11	1.4 \pm 0.22	1.9 \pm 0.21
Surface tension (γ , $\text{mN}\cdot\text{m}^{-1}$)	49 \pm 0.55	40 \pm 0.5	71 \pm 0.75	71 \pm 0.75

To compare with the results obtained by Hann et al. [7], measurements in the present study were obtained at the same axial location, i.e., 1600 mm from the inlet, as indicated on Figure 1. The experiments were conducted at the same gas and liquid velocities considered by Hann et al. [7]. In the present study, the liquid Reynolds number, Re_L , is defined as the volumetric liquid flow rate per unit span (loading factor, L_F) divided by the kinematic viscosity of the fluid (μ). The superficial gas velocity, V_G , is obtained by dividing the volumetric flow rate of the air by the cross-sectional area of the channel.

As a first step, the film statistics were measured for four gas velocities (20 m/s, 25 m/s, 30 m/s and 35 m/s) and four liquid flow rates (1 litre/min, 2 litre/min, 3.5 litre/min and 5 litre/min). These correspond to liquid Reynolds numbers of 105, 220, 360 and 520 respectively for the water and water-butanol cases, while for 2.5% water-glycerol cases they will be 50, 105, 185 and 265. For calculation of the film statistics only the highest viscosity and lowest surface tension solutions were considered. This is done so that only significant points are viewed on the graphs. Additional data was obtained for the G-W solutions giving liquid Reynolds numbers of 220, 360 and 520 for direction comparison purposes. The bubble spectra were then calculated only in the misting regime for various G-W and B-W solutions for the same Re_L of 220, 360 and 520 and gas velocity of 25 m/s, 30 m/s and 35 m/s.

Both the camera and the laser (DANTEC) were located below the bottom of the channel. The laser is projected over an area, as shown in Figure 1. The laser and the camera were synchronized, and the images were obtained at a frequency of 10 kHz for 1 second, thus giving 10,000 images. At this frequency, the total energy of the laser pulse is around 2.7 mJ. The maximum duration of the laser pulse was 100 ns, which is much smaller as compared to the characteristic time scale of the flow. The laser beam was uniformly spread over the region of interest (ROI). The camera captured a ROI of 44 mm \times 20 mm at a resolution of 1024 and 460 pixels in the longitudinal and lateral direction, respectively. This gives a spatial resolution of 43 μm /pixel.

The BBLIF technique was employed in the present study to obtain the film statistics and the bubble spectra. The BBLIF technique is based on the Lambert-Beer law, in which the thickness of the liquid film is correlated with the brightness of the liquid containing the fluorescent dye. A minute amount of fluorescent dye (Rhodamine 6G) was dissolved in the working fluid (15 mg/litre) for the use of this technique. It should be noted that such a small amount did not affect the properties of the liquid, and it was found that there was no significant difference before and after the addition of the dye. The liquid containing the dye is then excited with a Nd:YLF laser light having a wavelength of 527 nm, which is close to the maximum value of the dye absorption spectrum. The dye absorbs the laser light and re-emits in the red spectral domain, which is captured by the high-speed camera (IDT OS4). A low pass filter was mounted in front of the camera lens to curtail the entry of scattered/reflected laser light. The relationship between the local intensity, $J(x,y,t)$, and the film thickness, δ , is given by equation (1):

$$J(x, y, t) = C(x, y, t)[1 - \exp(-\alpha\delta(x, y, t))][1 + K \exp(-\alpha\delta(x, y, t))] \quad (1)$$

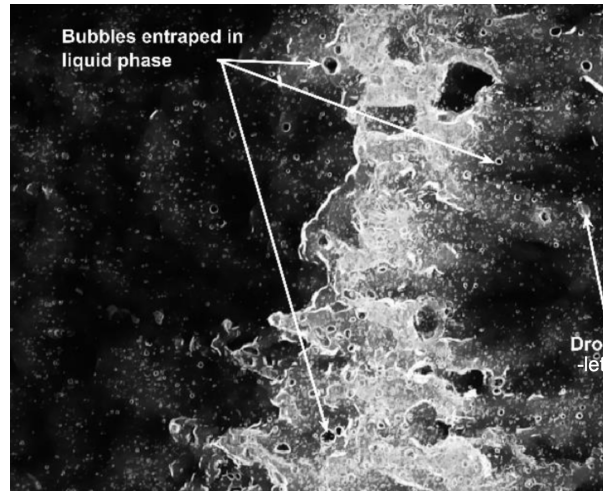
where α , K , and C denote the absorption coefficient of the fluorescent light, reflective coefficient of the liquid-gas interface, and the compensation matrix (to relate film thickness to fluorescent intensity and to compensate for the non-uniformity of the exciting light), respectively. All these quantities were obtained either from auxiliary experiments or during calibration. α is obtained by measuring the brightness of the liquid layer for different thickness, while the compensation matrix is estimated by the time-averaged fluorescence intensity captured by each camera pixel. Details about the calibration procedure and methodology for calculation of each of the above variables can be found in [17].

The main limitation of the BBLIF technique is the optical distortions due to the internal reflection created by steep interfacial slopes; these are most likely occur on the front of the fast ripples. **The strong reflection of both the laser and fluorescent light, which is unaccounted in equation (1) might lead to non-physical localized peak of film thickness magnitude. In order to reduce the contribution of such erroneous value into the measured film characteristics, the film thickness records were cut off at the level of 5 mm, which is above the maximum physical thickness of the waves for all the experimental conditions.**

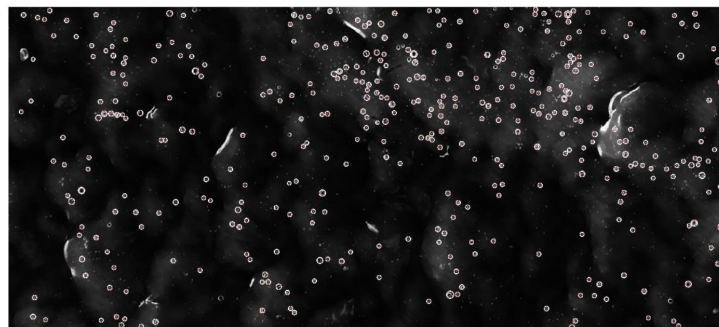
The primary source of the random error for the film thickness measurement is due to the camera noise. **This error was estimated by measuring the standard deviation of a temporal record of fluorescence intensity emitted by a layer of liquid of constant thickness. This noise amplitude is independent on signal level. For the brightness values corresponding to the thinnest base film (see below), the maximum relative error due to the noise is approximately 3%.** Moreover, the error due to the non-uniformity of the individual pixels after carrying out the compensation matrix procedure was also found to be $\approx 3\%$. Thus, the overall error of the film thickness measurement will be around 6%. Most of the distortions in an image are of small sizes, and are segmented by a 2D-median filter before the calculation of the instantaneous film thickness. In general, the size of the distortion sources (bubbles/droplets) is smaller than half of the area of the filter window. Hence the 2D-median filter will allocate a value, which will be the most probable, of the film thickness surrounding the feature. In the present study, the mean bubble size is around 180 μm , corresponding to an area of 14 pixels. This is significantly smaller than the filtering window (50×50) used in the present study. This confirms that the adjacent features do

not interfere.

3. Algorithm for bubble detection



(a)



(b)

Figure 2: Typical image (a) illustrating the different structures present in the flow. The flow is from right to left. (b) Successful implementation of bubble tracking algorithm (developed by G2TRC).

Figure 2a shows a typical image obtained using the BBLIF technique, from which the film thickness matrix, $\delta(x, y)$, can be obtained for each time step. The brightness of each pixel in Figure 2a is proportional to the value of the film thickness at that location. Moreover, from Figure 2(a), based on the brightness level, two different regions can be easily distinguishable: (I) a dark area, which represents the base-film, (II) a bright area, which represents the disturbance wave. Apart from these, other structures that are present in such a gas-sheared flow, such as liquid droplets, and bubbles entrapped in the liquid phase, are also visible. The flow direction is from right to left. The arrows mark an entrained droplet, and bubbles.

It is evident in Figure 2a that the number of bubbles inside the disturbance waves is much larger than that inside the base film. This difference is not only related to the thicker film inside the disturbance wave but also the number of bubbles per unit wall area also increases significantly. From Figure 2a, it is observed that a substantial amount of bubbles of different sizes are present in a single image. Thus, it became imperative to develop a tracking algorithm to detect all the bubbles from all the images

automatically. The two most common methods for circle detection are the geometric based method and appearance-based method. The Hough transformation (HT) is an example of the former, while the convolutional neural network (CNN) is based on the later. Though CNN is more accurate and superior to HT, it takes a colossal amount of computational time. Thus, a processing routine of both approaches is implemented in the present study in MATLAB[®], which consists of the following steps:

- Step 1: “imfindcircles” which is based on the Hough Transform is used to detect circles. In this case, three levels of detection were set. The first level detects diameters between 2 and 5 pixels, while the second and third levels detect diameters between 6 and 10 and 11 and 15 pixels respectively. The sensitivity used in the algorithm for MATLAB for the former is 88%, while for the latter it is 85%. To detect only the bright ridge lines of the bubbles, ‘Object Polarity’, ‘bright’ was applied.
- Step 2: The “Canny edge detection” technique was further used to identify edges of a feature. This complemented the detection in Step 1, to allow the detection of bubbles of all sizes. Repeated bubbles from step 1 are neglected in this step. Non-bubbles were filtered out using the property ‘Euler-Number’ (belongs to the ‘regionprops’ function in MATLAB). Moreover, false bubbles were removed by setting an appropriate magnitude for the threshold.
- Step 3: Once the bubbles were identified using the above method, duplicate bubbles were removed by finding the bubble centres. Moreover, any droplets which were detected as bubbles were removed by considering that their intensity is much higher than the surrounding. Finally, any features with eccentricity > 1 were also removed as this corresponds to non-bubbles.

The governing parameters of the algorithm were selected during extensive preliminary testing of the algorithm based on randomly chosen frames with different flow conditions and working liquids. The raw images with superimposed images of the identified bubbles (similar to the bottom part of 2b) were analyzed visually with manual calculation of the number of properly identified bubbles, compared to the number of false-positive and false-negative errors. The parameters specified above correspond to the smallest fraction of error events; these values were selected to be employed in the final version of the algorithm applied to the whole set of data. The result of applying the above algorithm can be seen in Figure 2b. From Figure 2b, it can be observed that the algorithm successfully captures most of the bubbles present in the image, irrespective of their size. By testing random images, it was observed that around 3 - 7% of the detected bubbles are false positives, and approximately 5 -12% bubbles were not detected. This means approximately 75-80% of the bubble identification is correct.

4. Characterization of the flow based on film statistics

When a liquid film flows in the presence of a *co-current* gas stream, the drag force between the gas and the film accelerates the film. Since the liquid flow rate remains constant, such an acceleration results in a reduction of film thickness. If the liquid flow rate is increased while the gas velocity is constant, the film gets thicker since it contains more liquid. At large enough gas and liquid flow rates, the liquid film consists of large-scale disturbance waves travelling with high speed over a thin “base film”

layer. Both base film and disturbance waves are covered with ripples, slow and fast respectively; these are all generated at the rear slopes of the disturbance waves as described in [18]. Increase in the gas velocity leads to a decrease in both base film thickness and disturbance wave height, but an increase in disturbance wave velocity and passing frequency. Increase in liquid flow rate leads to an increase in all the aforementioned characteristics. The distribution of liquid volume between the base film and the disturbance waves is a non-trivial process which depends strongly on the flow parameters and the physical properties of both phases. In this section, we analyze how change in liquid viscosity and surface tension affect the properties of both the base film and disturbance waves.

The analysis is carried out based on spatiotemporal matrices of film thickness, $\delta(x, t)$. Such matrices are obtained by stacking together all the instantaneous profiles of film thickness, $\delta(x)$, obtained at the same transverse coordinate, y , in consecutive moments of time. Three quantities can be easily obtained without identifying x - t trajectories of individual disturbance waves, namely, mean film thickness, base film thickness and velocity of disturbance waves. The mean film thickness, δ_M , is defined as the average value of the whole $\delta(x, t)$ matrix. The base film thickness, δ_B , is defined as the modal value in film thickness distribution since the base film occupies the main part of each film thickness record and it has a relatively low variation of film thickness, mainly due to the presence of small-amplitude slow ripple waves. The modal value was calculated for each temporal record of film thickness at given x and then averaged over all the temporal records. The average velocity of the disturbance waves, V , can be easily estimated in frames of cross-correlation analysis. For any pair of temporal records, $\delta(x_1, t)$ and $\delta(x_2, t)$, the position of the maximum of the cross-correlation function corresponds to the time required for a disturbance wave to pass the distance $(x_2 - x_1)$ and thus identify the velocity value. Due to their high amplitude, the disturbance waves make the largest contribution into the cross-correlation, and the time lag identified by the cross-correlations corresponds to their velocity. The total velocity for a given combination of flow conditions was estimated by averaging all the velocity values over all the possible pairs of x_1 and x_2 separated by a distance of 16 mm. This separation is chosen because it maximises use of the imaged area while avoiding the edges of the image.

The quantities outlined above are shown in Figure 3. The mean film thickness, δ_M , (Figure 3a) shows a very mild decrease with gas velocity and a stronger increase with liquid flow rate. This behaviour is the same for all the liquids, though for δ_M is significantly larger for both butanol and glycerol solutions in comparison to water. This difference is shown quantitatively in Figure 3b, where δ_M values for B-W and G-W solutions are plotted alongside those for water at the same liquid and gas flow rates. It is not surprising that a more viscous liquid shows higher film thickness values since the viscous force resists the momentum transfer from the gas phase to the liquid phase; thus, the more viscous liquid moves more slowly and, due to the constant flow rate, the film remains thicker. It is much less clear why the lower surface tension results in a thicker film, given that viscosity of B-W solutions and water are the same.

The base film thickness, δ_B , (Figure 3c) shows a more prominent effect of V_G and a weaker effect of liquid volume flow rate, Q_L in comparison to that of mean film thickness. Another difference is that δ_B values show much better separation between B-W and G-W; though for both solutions δ_B is higher than for water, the effect of lowering surface tension to 40 mN/m has less effect compared to the effect of

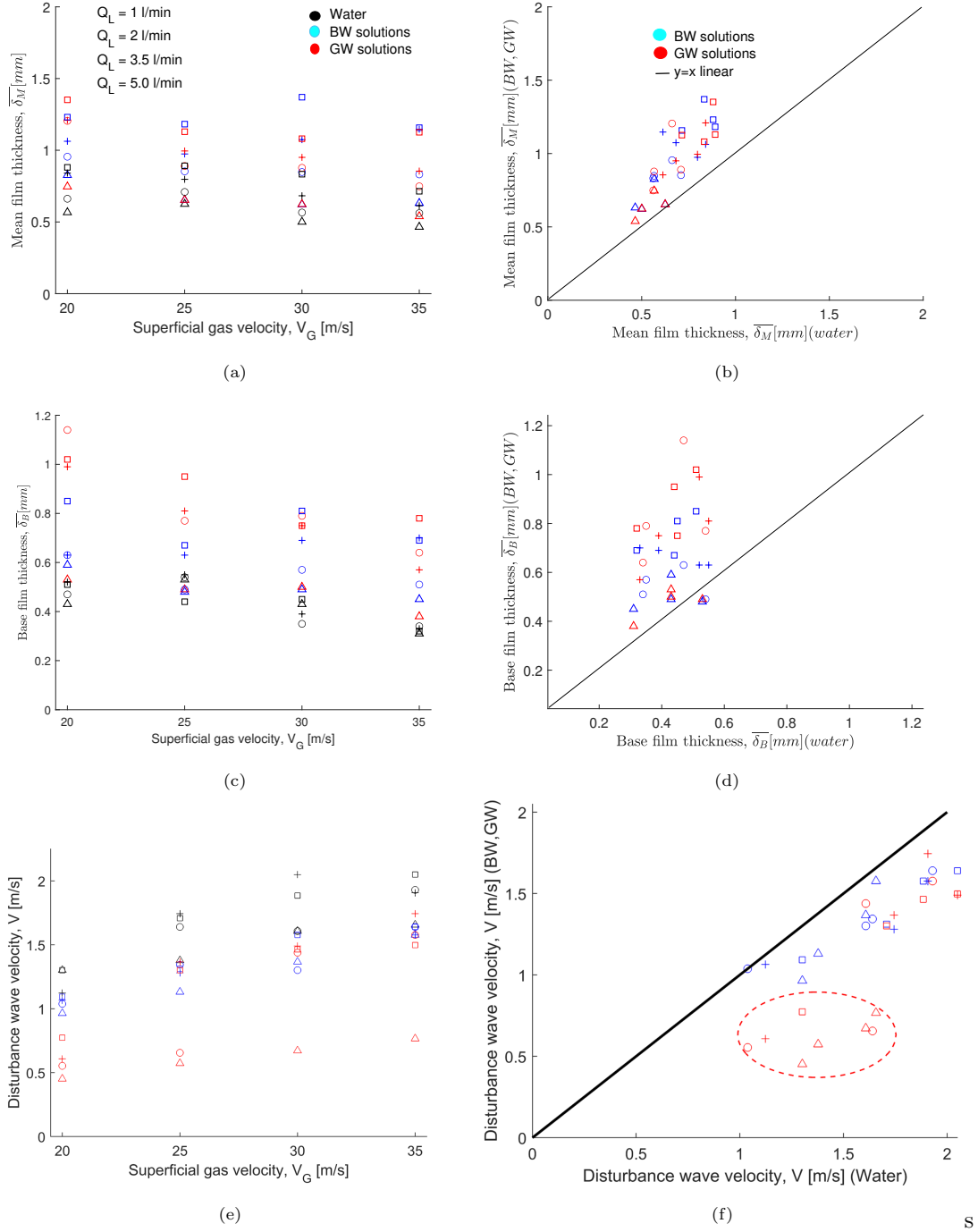


Figure 3: The effect of gas and liquid flow rates and liquid properties on mean film thickness (a, b), base film thickness (c, d) and disturbance waves velocity (e, f).

increasing viscosity to 1.9 cP. This is also illustrated in Figure 3d, which shows that increasing viscosity has more of an effect on the base film thickness than on the mean film thickness.

The disturbance wave velocity grows with both gas and liquid flow rates (Figure 3e). This means that the cause of increase in film thickness due to lower surface tension is related to the change of the disturbance waves' properties. In contrast to film thickness, wave velocity V is larger for water than for both B-W and G-W cases. This behaviour is in agreement with the above considerations on mass

balance in the liquid phase: water is better accelerated by the gas stream than the other liquids, and faster movement results in a thinner film. It is interesting that the velocity values for G-W cases at low gas and liquid flow rates as identified in Figure 3f are much lower than the rest of the data sets. Visual inspection of the relevant $\delta(x, t)$ plots shows that there are no disturbance waves in these regimes for G-W cases, and the measured velocity corresponds to that of small-scale waves. This suggests that for these parameters the flow is no longer in the disturbance wave regime but has shifted to the 3D wave regime.

After the transition to the disturbance wave regime, the velocity values lie quite close to each other for different values of Q_L . It was noticed that a similar but quantitatively weaker velocity decrease can be observed for water at the lowest Q_L and V_G . Similarly, B-W results all lie close to each other, suggesting that unlike the G-W results, a decrease in the surface tension does not transfer the flow to another regime. It can be concluded based on both velocity data and the visual analysis of film thickness records, that low surface tension facilitates the transition to disturbance waves, whilst higher viscosity dampens this transition. Figure 3f compares the velocity values between the different liquids. When the disturbance waves are dominant in the film wave structure, the effects of increased viscosity and reduced surface tension are coincidentally almost the same. For the flow without disturbance waves (points encompassed by the dashed ellipse) velocity values correspond to a different type of waves that are much slower than the disturbance waves.

Further analysis of wave frequency, amplitude and longitudinal size requires identification of spatio-temporal trajectories of individual disturbance waves in the $\delta(x, t)$ matrix. Different identification algorithms have been employed in a number of recent papers ([17, 19, 20]); in this paper, we use a simplified version of such an algorithm, under the assumption that all the disturbance waves move with the same velocity, V . Thus, the whole matrix $\delta(x, t)$ can be converted into a vector using equation (2):

$$\delta_V(t) = \frac{1}{X} \sum_{x=1}^X \delta(x, t + \frac{x}{V}) \quad (2)$$

For simplicity, the $\delta_V(t)$ dependence does not include two triangular fragments at the beginning and the end of $\delta(x, t)$ with dimensions X by X/V . An example of $\delta_V(t)$ dependence is shown in Figure 4(a). The original $\delta(x, t)$ matrix is shown in Figure 4(b). The disturbance waves in such a matrix look like stripes of large film thickness with a gradient relative to the t-axis; if the gradient is larger, the wave velocity is larger.

The regions between the disturbance waves (the base film) are noticeably thinner, and contain narrow stripes of different gradient corresponding to slow ripples. The disturbance waves are distinguishable as high peaks in δ_V , due to their high amplitude and velocity close to V . An arbitrary threshold based on the value of δ_B was set to identify individual disturbance waves. An additional manual selection was employed, in order to ensure proper identification and discarding of doubtful peaks. Secondary peaks may appear due to the presence of slow ripples, which may travel with high speed behind the disturbance wave for some time, or due to the appearance of the side edges of proper disturbance waves along the investigated line. The main criterion for selection was the stable behaviour of a disturbance wave through

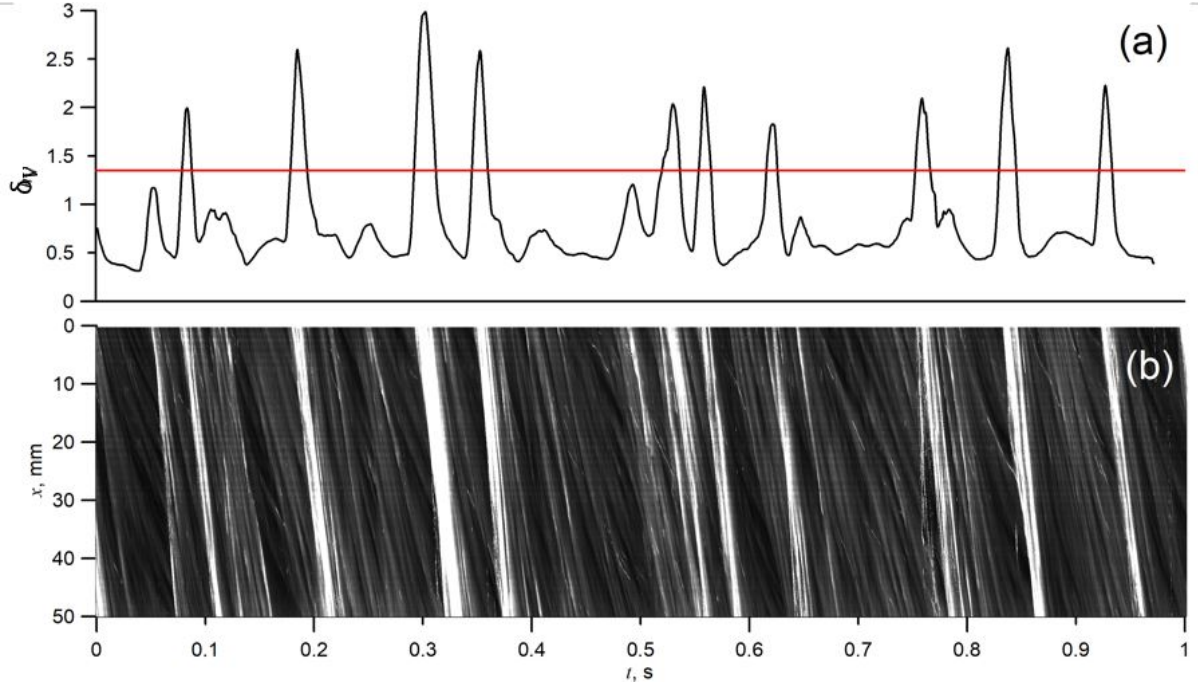


Figure 4: a) An example of $\delta_V(t)$ array obtained as a result of averaging of film thickness along a constant-speed trajectory. The red line shows a threshold value equal to $3\delta_B$. (b) The full $\delta(x,t)$ matrix for the same set of flow conditions (water, $Q_L = 5$ l/min, $V_G = 30$ m/s).

the whole length of the region of interest.

After the peaks are detected, the frequency of the disturbance waves is defined as the number of peaks in the time period of the record, with a minor correction for the shorter length of δ_V in comparison to that of $\delta(x,t)$. The mean amplitude of the waves, A , is defined as the average height of all detected peaks with the subtraction of the base film thickness. The mean longitudinal size of the waves is defined as the average temporal duration of a wave in δ_V at a level higher than $\delta_B + 0.2A$, multiplied by wave velocity, V . It should be noted that usage of the same velocity value for processing all the individual waves is a simplification leading to a certain measurement error for $\langle A \rangle$ and $\langle L \rangle$. Indeed, if the velocity of an individual wave is different from $\langle V \rangle$, it would be shifting relatively to the presumed spatiotemporal trajectory during the processed time span. As a result, the time-averaged shape of such a wave will get blurred, yielding underestimated amplitude and overestimated longitudinal size. However, quantitative estimation of the error based on time-averaging of a model shifting wave indicates that due to small size of region of interest and low standard deviation of the velocity distribution, the error in average values of A and L would not exceed a few percent. Moreover, this simplification is expected to affect the measurements for different liquids in the same manner; thus, the comparison will be even less sensitive to this source of error. The results of the measurements are shown in Figure 5.

The frequency of the disturbance waves is strongly influenced by V_G in a linear manner (Figure 5a); it also increases with liquid flow rate. As expected, for the glycerol solution and low-velocity conditions (see the dashed ellipse in Figure 3f), the frequency of the disturbance waves is zero; obviously, neither amplitude nor length of disturbance waves is reported for these cases. For all cases where disturbance

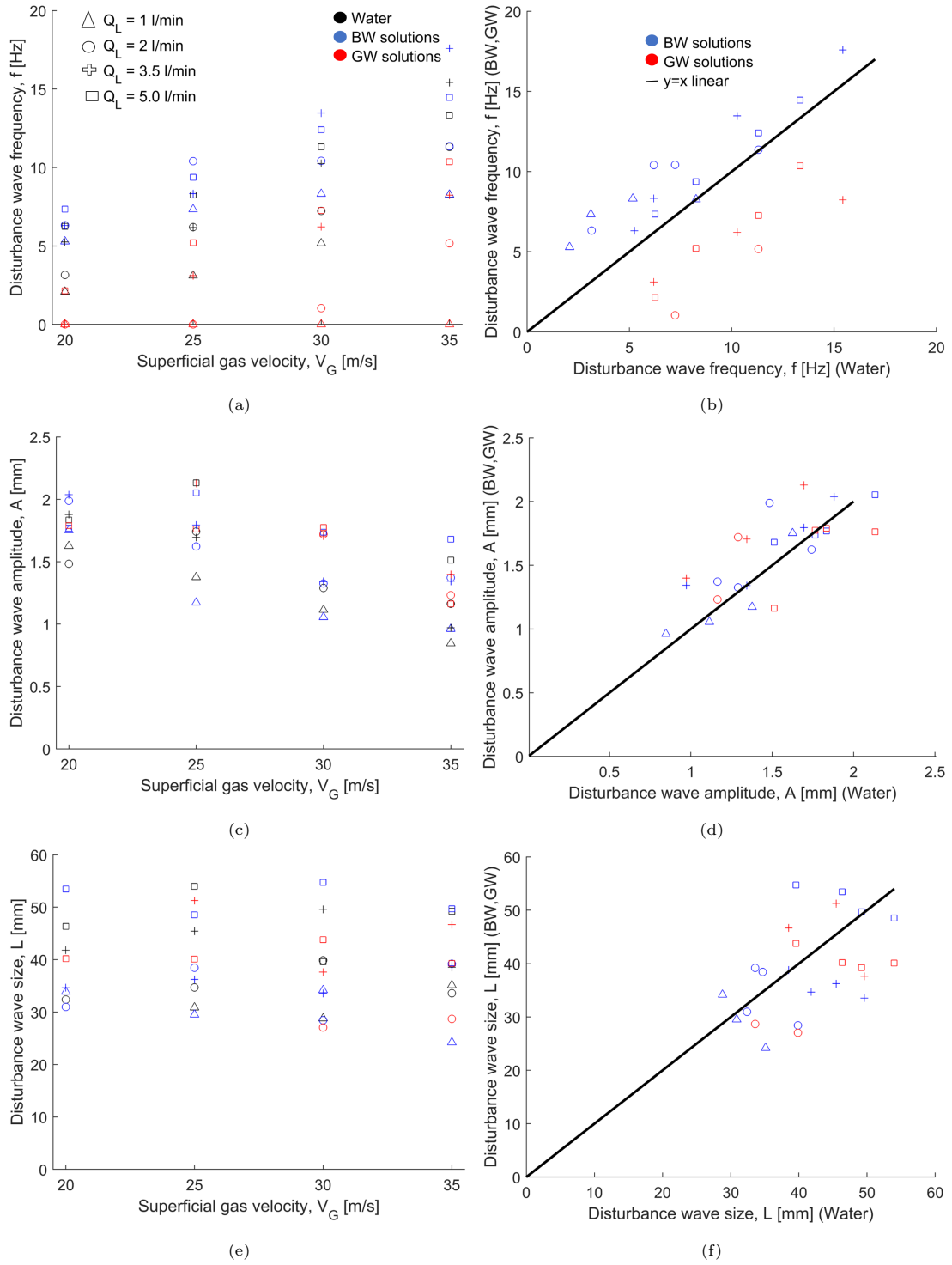


Figure 5: The effect of gas and liquid flow rates and liquid properties on disturbance wave frequency (a, b), amplitude (c, d) and longitudinal size (e, f).

waves are present, increase in viscosity results in lower wave frequency if the liquid flow rate is the same (Figure 5b). At the same time, decreasing the surface tension results in disturbance waves with a higher frequency. It is interesting to note that frequency and velocity are usually closely related to each other. If the spatial distance between the waves is constant, faster waves would appear at the measurement

position more frequently. Judging from a comparison of Figure 3f and Figure 5b, this might be the case for the water-glycerol solution. It is likely that the distance between the disturbance waves is of the same order for water and G-W, but the frequency is lower for a more viscous liquid since the wave moves slower. However, for B-W solutions, the disturbance waves' frequency is higher than for water, despite the fact that the velocity has decreased. Thus, lower surface tension leads to a strong decrease in spacing between the disturbance waves, making the film surface much more agitated. Both amplitude and longitudinal size of the disturbance waves (see Figure 5c and Figure 5e), decrease with gas velocity but increase with liquid flow rate; the amplitude is slightly more sensitive to change in V_G .

As for the effect of working liquid properties on disturbance wave amplitude A and size L (Figure 5d and Figure 5f), it is difficult to say anything certain. The values tend to group around the ' $y = x$ ' line with a large scatter of 20-30% and without any prominent tendency. It could only be said that the amplitude values for water are on average slightly lower than for the two other liquids, whilst for the longitudinal size, the situation is the opposite. In other words, the disturbance waves tend to be slightly steeper at either higher viscosity or lower surface tension. The scatter of the values between the different runs is largely due to the small number of disturbance waves in each run. Still, it can be concluded that the liquid properties within the investigated range do not exert any drastic systematic influence on amplitude and longitudinal size of disturbance waves. At the same time, the effect of liquid properties on frequency, velocity and film thickness are well-pronounced.

The effects of surface tension observed in the present experiments are opposite to those observed by Rivera et al. [13]. All the parameters related to film thickness (mean and minimum film thickness, amplitude of disturbance waves and ripples) decrease with reduced surface tension in the experiments of Rivera et al. In our case, mean and base film thickness are definitely larger for B-W cases than for water and the disturbance wave amplitude tends to be slightly higher. At the same time, the disturbance wave frequency increases at lower surface tension in our experiments but decreases in [13]. Velocity and longitudinal size of the waves were not measured in [13].

The most plausible explanation of this discrepancy, assuming that both measurement techniques work with acceptable reliability, is that the measurements were conducted in dissimilar geometries. The experiments of Rivera et al. were conducted near the end of a 5m-long pipe with inner diameter of 44mm whereas our measurements were conducted 1.6m along a rectangular duct. The hydraulic diameters are nearly the same in both cases, but the distance from the inlet in our experiments is about 3 times shorter. It could be expected that further downstream the entrained fraction would be much larger; hence, film flow rate would be lower. Since lower surface tension would obviously facilitate droplet entrainment, this effect would be more pronounced further downstream and might overcome the effects we observe at 1.6m from the inlet. Nevertheless, this discrepancy warrants additional investigation.

The main goal of this paper is to study the effect of liquid properties on bubble production. The most useful conclusions of the film and waves analysis for this purpose are:

1. With both alternative liquids, larger film thickness, and hence, more liquid volume to contain gas bubbles, is expected. In addition, due to lower liquid velocity the bubbles are also expected to be less prone to collapse.

2. The fraction of film occupied by the disturbance waves ('intermittency'), defined as ratio of longitudinal size of a wave to the spatial distance between adjacent waves, is close to each other for water and G-W cases but noticeably higher for B-W cases.
3. For G-W cases at low gas and liquid flow rates, no disturbance waves could be observed suggesting that in G-W cases the flow has shifted to a different flow regime. For water these conditions are within the transitional range. Since the bubbles are expected to be predominantly produced by impacting droplets previously torn from disturbance waves, it would be reasonable to study the bubbles only in conditions where disturbance waves are significant. Hence, the bubble studies will be limited to the range of $V_G \geq 25$ m/s and $Q_L \geq 2$ l/min (i.e. $Re_L \geq 220$). Moreover, we will also relate G-W cases to water through constant liquid Reynolds number instead of the flow rate, to ensure the presence of disturbance waves in the whole regime matrix.

5. Characterization of the flow based on bubble dynamics

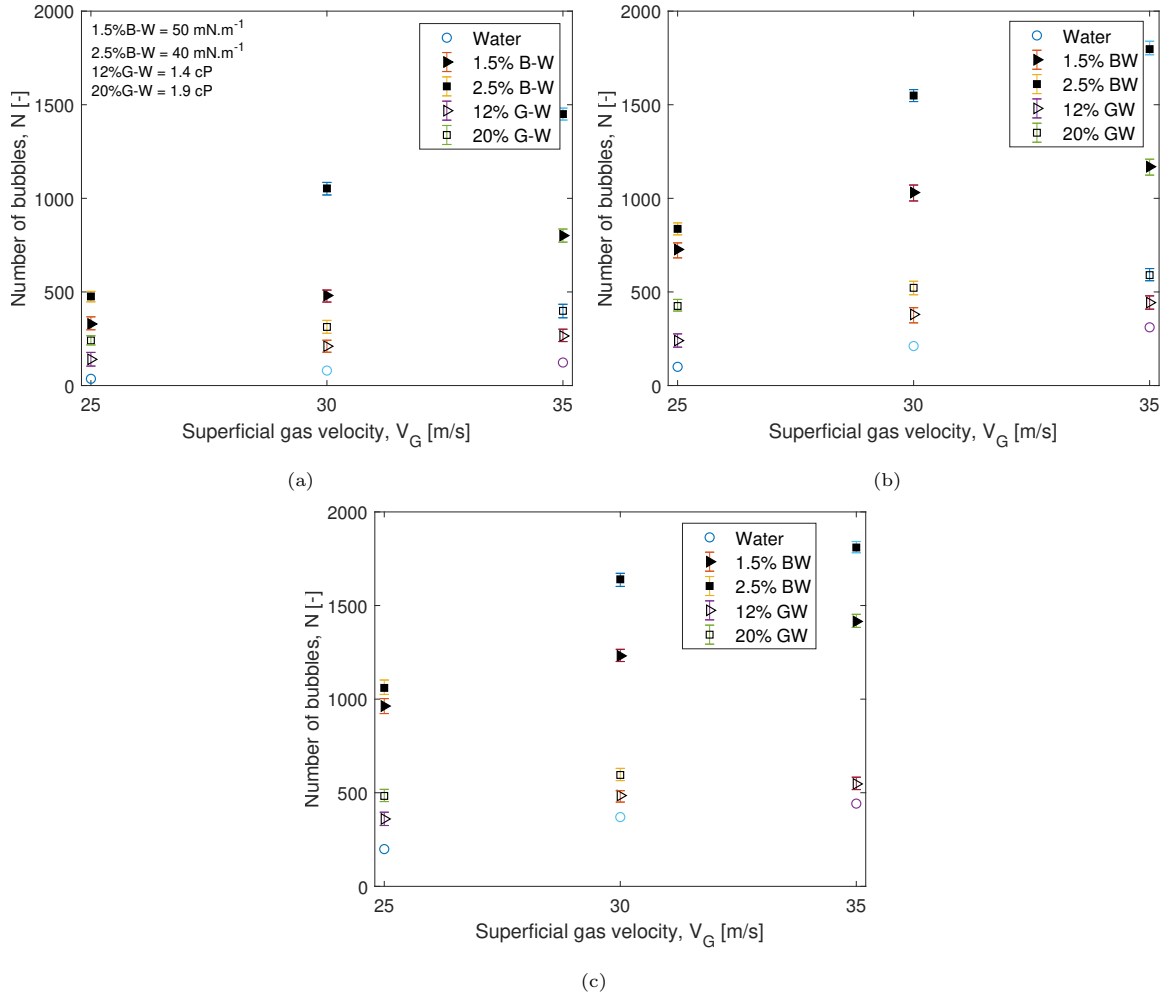


Figure 6: Time-averaged bubble count (N) for different solutions at various liquid and gas flow rates (a) $Re_L = 220$ (b) $Re_L = 360$ (c) $Re_L = 520$. The bubble count for the B-W solutions is highest, followed by the G-W solutions.

Figure 6 shows the time-averaged bubble count, N , for various investigated aqueous solutions at

different gas and liquid flow rates. This enables a direct comparison with the results of [7], which were for water. It is evident from Figure 6 that regardless of the liquid and gas flow rate, with a decrease in liquid surface tension, and increase in viscosity, the number of bubbles generated per image is higher as compared to the bubble count of water. Despite of the quantitative difference among the various solutions in terms of bubble count, the hydrodynamic phenomenon for all the cases will be qualitatively the same. Phenomena such as disturbance waves, bag and ligament break-up, and interaction between the impacting droplets and the wavy gas-sheared liquid film was observed for all the cases in the present study as was previously observed for water [6].

Entrainment occurs due to the deformation of the liquid surface by the gas shear, while surface tension forces resist this deformation. Thus, at lower surface tension, entrainment will be stronger. Consequently, this will result in a higher number of entrained droplets in the gas core. These droplets, while interacting with the liquid surface, result in the formation of bubbles. With the decrease in surface tension from 70 mN/m (water) to 50 mN/m (1.5% B-W), more droplets are formed, as the cohesive forces at the interfaces will reduce, hence more bubbles. It is also possible that more bubbles will be created by a single-droplet impact, since the resistance through interfacial deformation will be weaker.

In our opinion, there are two main reasons for the increase in bubble count with an increase in viscosity. First, we compare the flows at the same Re_L , which implies the liquid flow rates are actually 1.4 and 1.9 times larger for more viscous liquids; so there is physically more liquid to be entrained. Second, viscous force would dampen the bubble collapse, since it ‘holds’ them tighter and does not let them to reach the interface as fast.

From Figure 6, it can be concluded that halving the surface tension, has a more significant effect on the bubble count than by doubling the viscosity. Secondly, it was observed that with increasing Re_L , the gradient of the bubble count with gas-velocity was found to increase.

Bubbles come in a variety of sizes, thus, it is useful to plot the distribution of the bubble sizes for all the aqueous solutions used in the present study. Rodriguez and Shedd [8] and Hann et al. [7] compared the bubble size distribution for various liquid and gas flow rates by normalizing the bubble diameter by the film thickness and plotting the bubble count in log scale. In Figure 7, the bubble size distribution for various liquid Reynolds number at $V_G=25\text{m/s}$ was plotted in the same way. The bubble distribution shown in Figure 7, follows an exponential decay trend, $N = N_0 \exp^{-E \frac{D}{\delta_M}}$. The same observation was also found in [8, 7]. However, it is found that not using the film thickness to nondimensionalise bubble size gave similar gradients for the different data sets as shown in Figure 8 and Figure 9.

Figures 8 and 9 show that for all the aqueous solutions, at a particular V_G , the bubble count increases with an increase in Re_L . It is also observed from Figures 8 and 9, that there are more small bubbles as compared to larger bubbles. There is a high probability that a large number of smaller bubbles are generated, and smaller bubbles have a higher probability of survival in the base as compared to the bigger bubbles after the disturbance wave has passed. The reason for this postulation is that in these experiments, the sizes of the ligaments are small, which results in small furrows once deposited into the liquid. This leads to entrapping of a small amount of air; hence smaller bubbles.

From Figures 8a - 8c, it is observed that the ratio of the number of small bubbles to larger bubbles

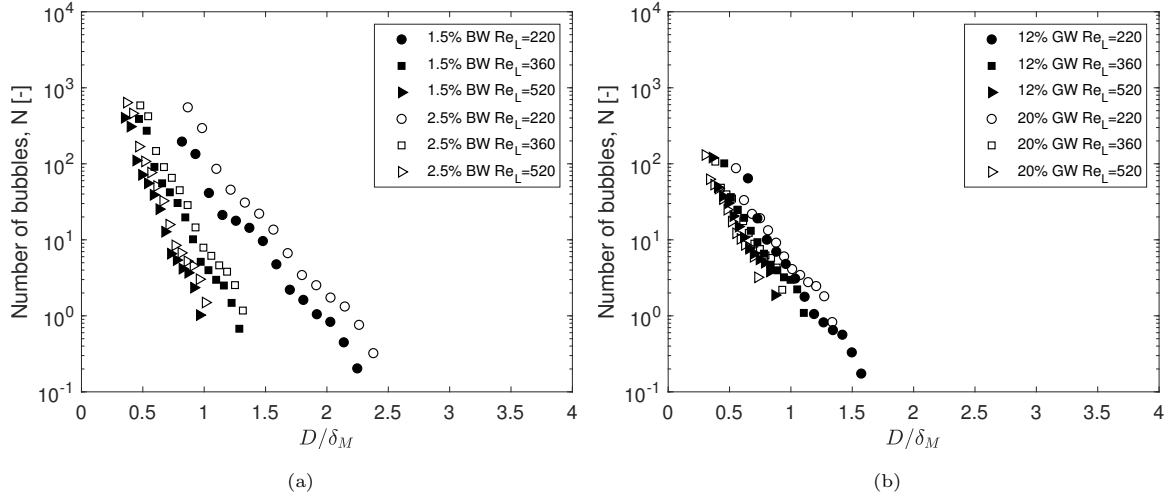


Figure 7: Bubble size distribution for various liquid Reynolds number and $V_G=25\text{m/s}$ for (a) different liquid surface tensions (b) different liquid viscosities. The abscissa axes are normalized by the mean film thickness. The ordinate axis is log-scale.

decreases as we decrease the surface tension (gradient becomes shallower). This is probably because of the formation of a higher number of droplets due to the reduction in the cohesive forces. Similarly, from Figures 9a - 9c, it is observed that the ratio of the number of smaller bubbles to larger bubbles decreases with increase in viscosity. Pancholi et al. [21] also observed that increasing the viscosity gives rise to a higher number of smaller bubbles. Moreover, it is observed that the bubble size distribution at higher gas and liquid flow rates for two different B-W concentrations are approximately the same; however, at low Re_L , the distribution is disparate. This indicates that the number of events of bubble formation and collapse is almost the same at high V_G and Re_L , and depends very little on the concentration of B-W. For the G-W liquids, this disparity is not obvious. The above observation can be substantiated from Figure 11, which shows the quantile-quantile plot for various solutions at different V_G and Re_L .

Using a similar methodology that used for the data in Figure 7, the exponential decrease of bubble size is also observed in Figures 8 and 9. The exponential decay in the equation, $N = N_0 \exp^{ED}$ was calculated for all the cases investigated in the present study. The exponential decay is highlighted for 1.5% BW and 12% GW at $Re_L = 520$ for various gas velocities in Figures 8 and 9 respectively. The exponential decay (E) for all the cases is shown in Figure 10. It is observed that the value of the exponential decay E varies within the uncertainty values with increase in Re_L for both B-W and G-W cases except for 1.5% B-W and 12% G-W at $V_G=25\text{ m/s}$. A decrease in the exponential magnitude indicates that the distribution is shifting towards the larger bubble size. The exponential shape of the bubble size distribution is due to the higher probability for the smaller bubbles to be created and survive in the base-film [7].

Quantile-quantile (Q-Q) plots are used to compare the bubble size distribution for two different concentration strengths at the same V_G and Re_L . A Q-Q plot is a non-parametric approach to comparing two probability distributions by plotting their quantiles against each other. In Figure 11, the data points are shown using a circular marker (blue). and the reference lines are used to highlight the similarity in the distribution. If the blue marker is offset from the straight line, it means they are of the same shape but shifted linearly.

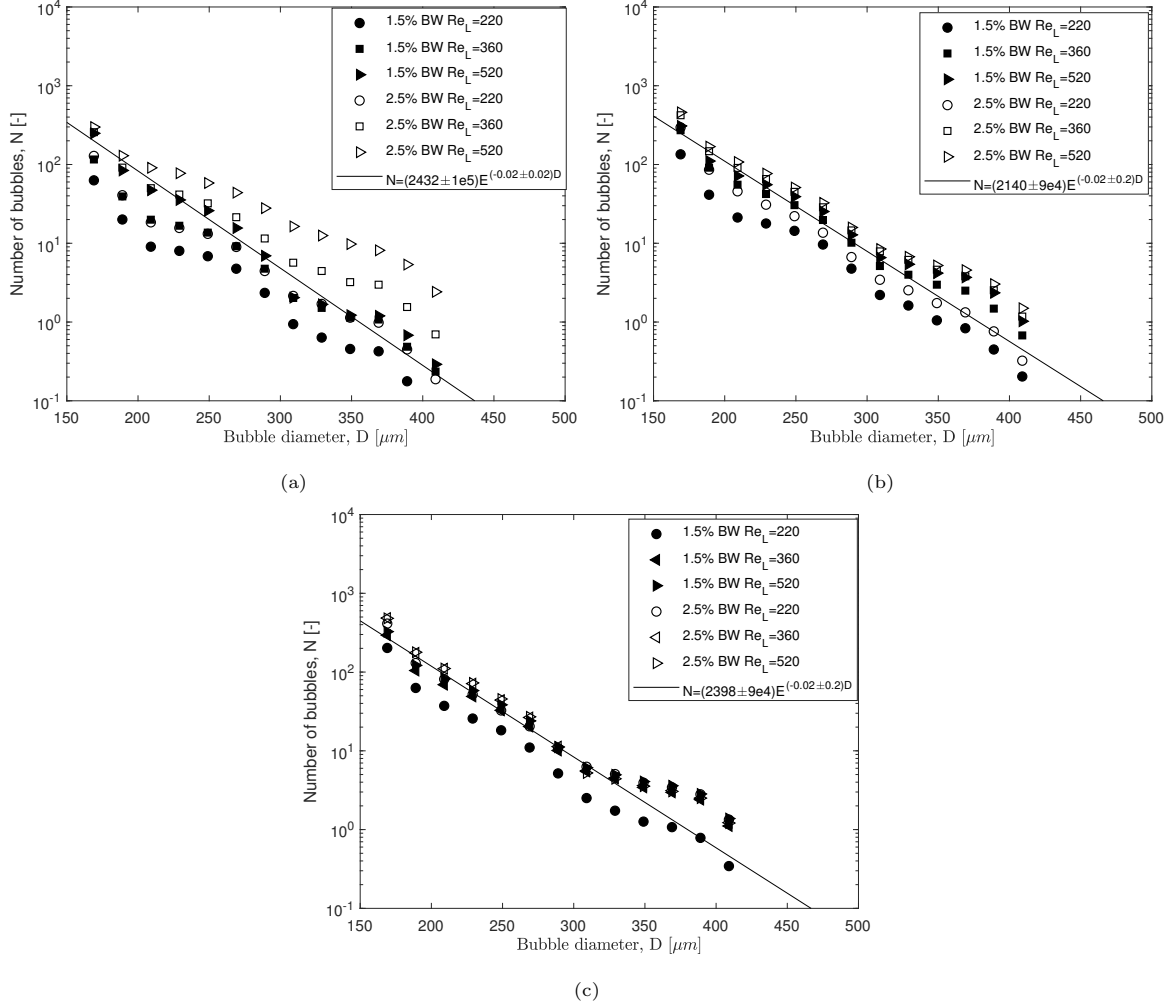


Figure 8: Bubble size distribution for various B-W concentration and Re_L at different gas velocities, $V_G =$ (a) 25 m/s (b) 30 m/s (c) 35 m/s. The ordinate axis is in logarithmic scale, N is the total number of bubbles/total number of frames.

From Figure 11a, which compares bubble size distribution between gas velocity 25 m/s and 30m/s for 1.5% butanol and $Re_L = 360$, it is observed that the data points on the Q- Q plot are mostly on the straight red line (shown between 16% and 84%). This indicates that the bubble size distribution is almost the same. This substantiates our observation relating to Figure 8. Figure 11b compares 1.5% butanol (lower surface tension than water) with 12% glycerol (higher viscosity than water) at a gas velocity of 25 m/s and $Re_L = 360$. As we move to the higher diameter quantiles for the butanol case the data skews away from the straight line relationship indicating that the size distribution is more skewed towards smaller bubbles in the butanol case.

Hann et al. [7] reported that the majority of the bubbles are present in the disturbance wave; this suggests that there can be a relationship between the number of bubbles and the volume of fluid (V_F) in the region of interest (ROI). To investigate this, both of these the parameters were plotted against each other. The volume of fluid (V_F) in the ROI for an image is calculated by multiplying the average film thickness with the area of interest. Figure 12 shows the relationship between the bubble count and the V_F for two of the solutions at $V_G = 25$ m/s and three of the flow rates. A similar linear relationship

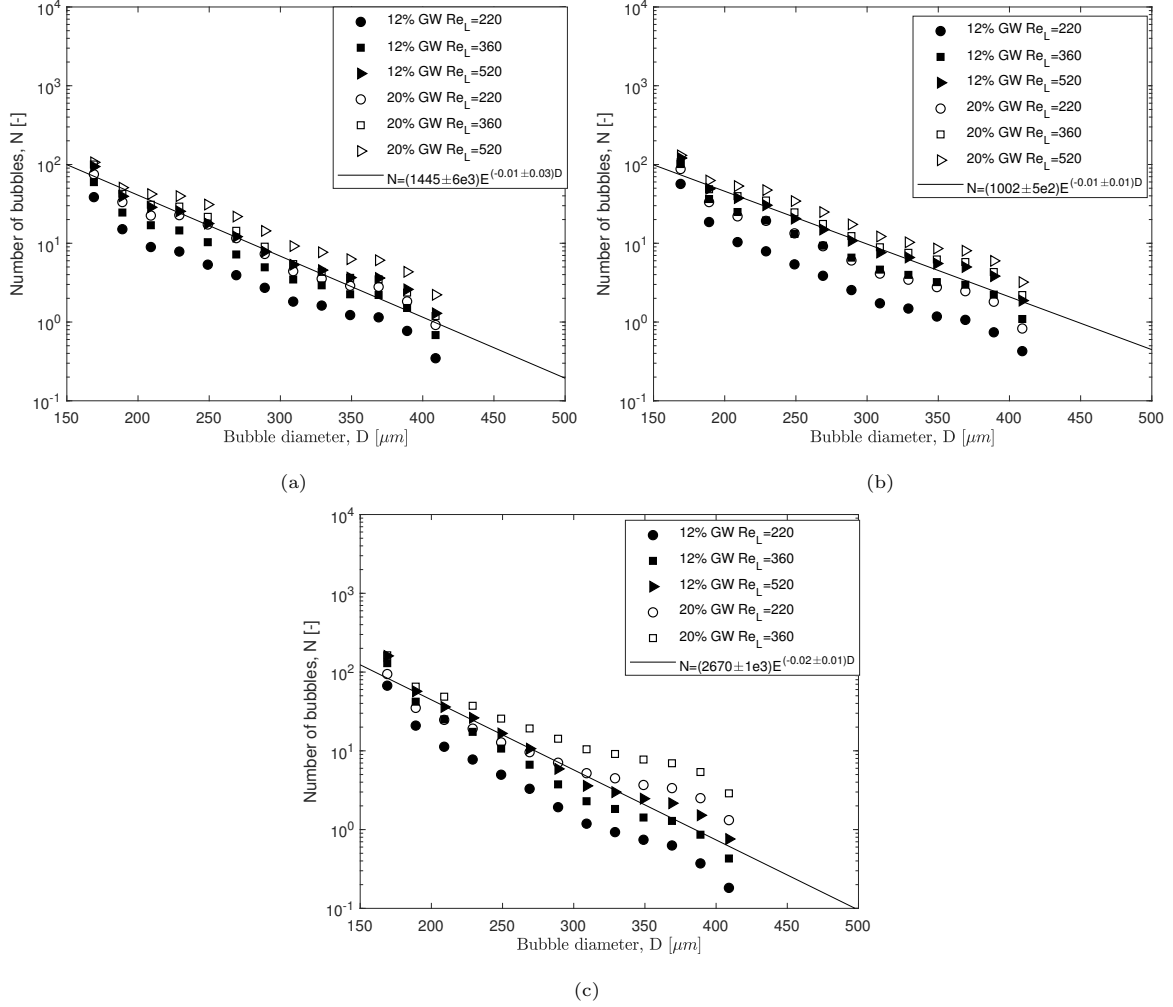


Figure 9: Bubble size distribution for various G-W concentration and Re_L at different gas velocities, $V_G =$ (a) 25 m/s (b) 30 m/s (c) 35 m/s. The ordinate axis is in logarithmic scale, N is the total number of bubbles/total number of frames.

between bubble count and fluid volume is observed here as in [7]. This is expected as the rate of liquid entrainment in the gas core increases with increase in Re_L , which in turn increases the number of droplets creating bubbles in the film. Qualitatively, it can also be observed from Figure 12, for the B-W case, that the gradient is increasing with the increase in Re_L . However, in comparison with the B-W case, the increase in the gradient with increase of Re_L for the G-W case is clearly identifiable but not as steep.

The temporal records of the volume of fluid and bubble concentrations were plotted to better understand the effect of disturbance waves on the bubble spectra. The presence of disturbance waves will create a well-defined hump in the V_F and bubble count, as shown in Figure 13. This correlates with Figure 12 showing that bubble count and volume of fluid are directly related. Figure 13 shows the temporal record of the superimposed V_F and N , at $V_G = 25\text{m/s}$ and $Re_L = 220$ for both B-W and G-W. A strong correlation between the V_F and N shows that a higher number of bubbles are present inside the disturbance waves. This confirms that the tracking algorithm is working effectively, as the profile of the number of bubbles detected is consistent with the volume of fluid profile. Moreover, it also confirms our previous qualitative observation that a higher number of bubbles is present in the disturbance waves.

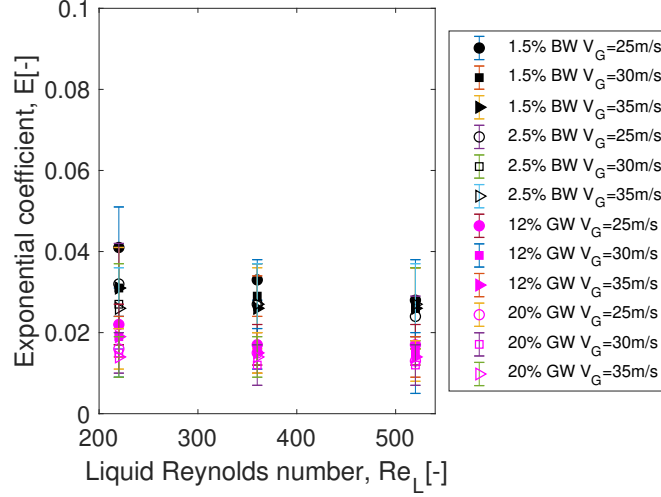


Figure 10: Shows the magnitude of exponent E from the exponential fit for all cases investigated.

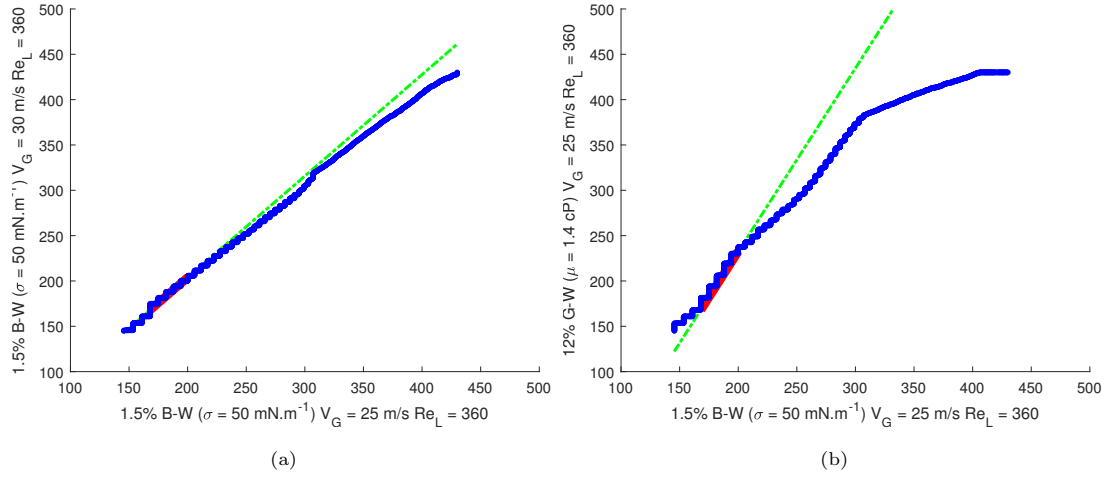


Figure 11: Quantile-quantile plot of the bubble size distribution V_G and Re_L (a) 1.5% BW $V_G = 25$ m/s between $V_G = 25$ m/s and 30 m/s (b) between 1.5% BW and 12% GW at $Re_L = 360$ and $V_G = 25$ m/s. The bubble diameters are in μm .

Further analysis was carried out by comparing the shape of the bubble size distribution inside and outside the disturbance waves. Bubbles were considered to be present inside the disturbance waves if the bubble count at a particular time instant is more than the time-averaged bubble count. The data obtained is shown in Figure 14 with number of bubbles plotted against bubble diameter for the base film and disturbance waves. Looking at Figure 14a for $D > 0.25$ mm the slope of the bubble size distribution inside the base film and disturbance wave is similar but there is a smaller proportion of smaller bubbles ($D < 0.25$ mm) in the disturbance waves. The similarity of distribution indicates that the bubbles inside the base film and disturbance waves are of the same origin. Small bubbles are primarily created by the oblique impact of the droplets. These bubbles travel inside the base film until a disturbance wave overtakes and keep them inside it. A similar distribution was observed for the G-W case although here the proportion of bubbles less than 0.25 mm in diameter increases in the disturbance waves as shown in Figure 14b.

To measure *aeration* in the fluid, it was assumed that the bubbles are spherical in shape. A numerical

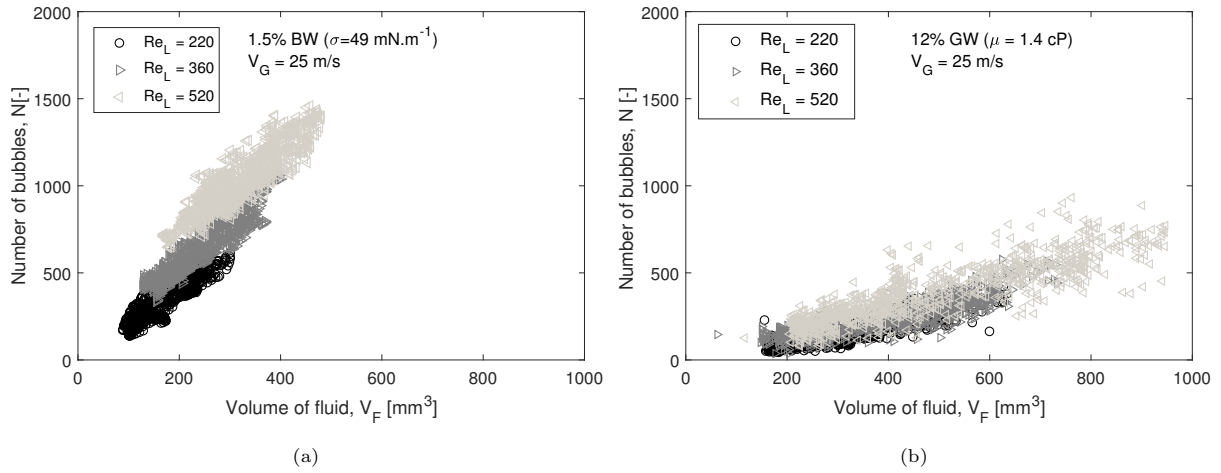


Figure 12: Linear relationship between the number of bubbles (N) in each frame and the corresponding volume of fluid (V_F) (a)1.5% BW for various Re_L (b)12% GW for various Re_L .

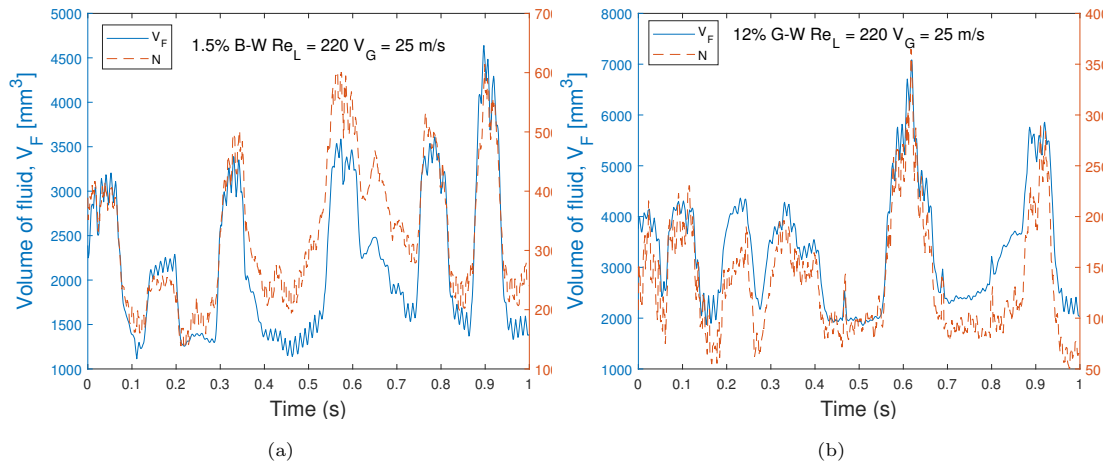


Figure 13: Temporal record of the bubble count and volume of fluid at $Re_L = 220$ and $V_G = 25\text{m/s}$ for (a) 1.5% BW (b)12% GW solution. The simultaneous increase in the volume of fluid and bubble count confirms the linear relationship and the accuracy and robustness of the bubble tracking algorithm.

value for *aeration* is obtained by summing the volume of all the bubbles in all the frames divided by the volume of fluid of all the frames. Figure 15 shows that the level of aeration increases with the increase in liquid flow rate and gas velocity. This is expected because, with the increase in Re_L and V_G , the frequency and amplitude of the disturbance waves also increases; consequently, the number of bubbles and the fraction of larger bubble generated increases. While, the increase in aeration with gas velocity is approximately linear, when we compared, the percentage of aeration between B-W and G-W solutions, it was observed that the effect of decreasing surface tension is more dominant as compared to the increase in viscosity.

The average aeration across the entire set of liquid and gas flow rate data for two liquid surface tension values is shown in Figure 16a, while Figure 16b shows the same for the two liquid viscosities. The average aeration at a particular surface tension is obtained by summing the aeration magnitude for all gas and liquid flow rates and then dividing it by the number of gas-liquid data sets. The same

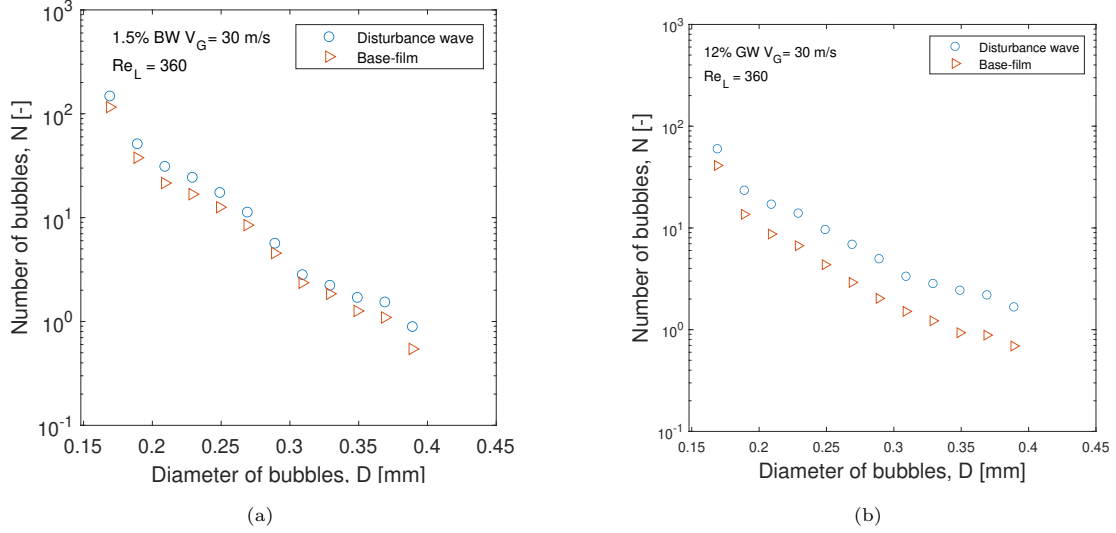


Figure 14: The bubble size distributions inside a disturbance wave and base film at $Re_L = 360$ and $V_G = 25\text{m/s}$ for (a) 1.5% BW (b)12% GW solution.

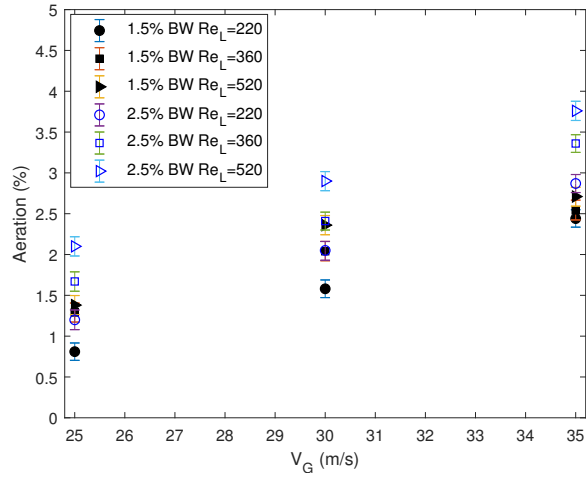
procedure was done for each liquid viscosity value. The aeration magnitudes for water are obtained from [7]. Assuming that the variation between surface tension and aeration is linear, it was observed that a 30% decrease in surface tension would lead to more than 300% increase in aeration. However, a 40% increase in viscosity will lead to approximately 33% increase in the aeration. This shows that reduction in surface tension can dramatically change the number of bubbles; which has implications for the heat transfer processes inside the film. The maximum and minimum aeration at a particular liquid surface tension is also shown in Figure 16.

Investigating the bubble velocity distribution is more complicated and is done by using a particle tracking velocimetry technique. The displacement distance between the same bubble in two consecutive frames was obtained, and the velocity of that individual bubble could be calculated since we know the time difference between the individual images. It is observed from Figure 17a, where gas velocity is constant at 25 m/s and surface tension is changed, that with the decrease in surface tension, the velocity of the bubbles increases. This can be confirmed by the dimensional plot of the effect of gas velocity, as shown in Figure 17b where surface tension is fixed and two gas velocities are compared. From Figure 17b, it is observed that with the increasing gas velocity, the bubble velocity also increases, since the film is moving faster.

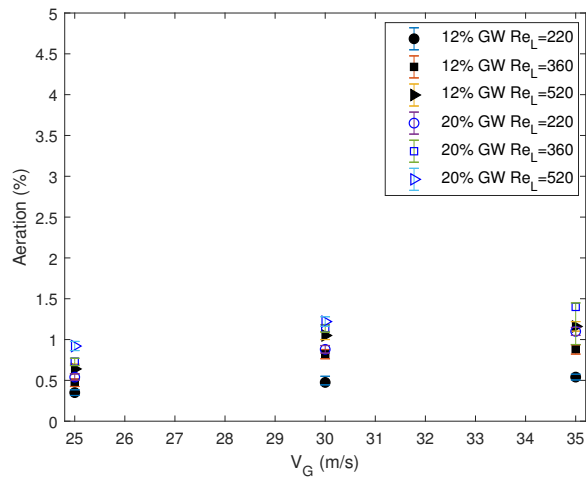
Similar observations can also be made for the viscosity cases shown in Figures 17c and 17d. From Figure 17c, it is observed that with the increase in liquid viscosity, the bubble velocity decreases. This is due to the increase in the resistance created by the liquid film.

6. Discussion of the above results in view of the heat transfer process

The work here has shown that the number of bubbles generated in a gas-sheared flow is dependent on both the surface tension and the viscosity. From observation of the images, the increase in bubble formation is related to the increase in the number of droplets shed from the surface of the waves. The

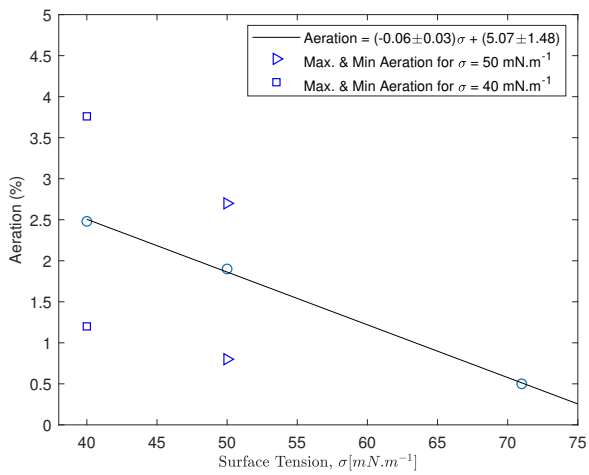


(a)

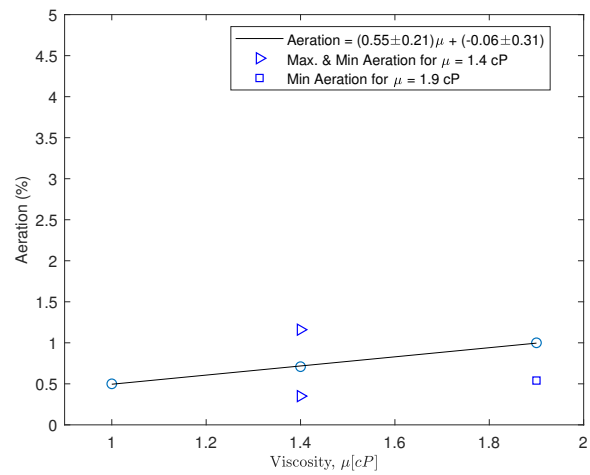


(b)

Figure 15: Increase in aeration with the increase in liquid and gas velocity. a) B-W cases (b) G-W cases.



(a)



(b)

Figure 16: Empirical linear relationship developed between aeration and (a) surface tension; (b) viscosity.

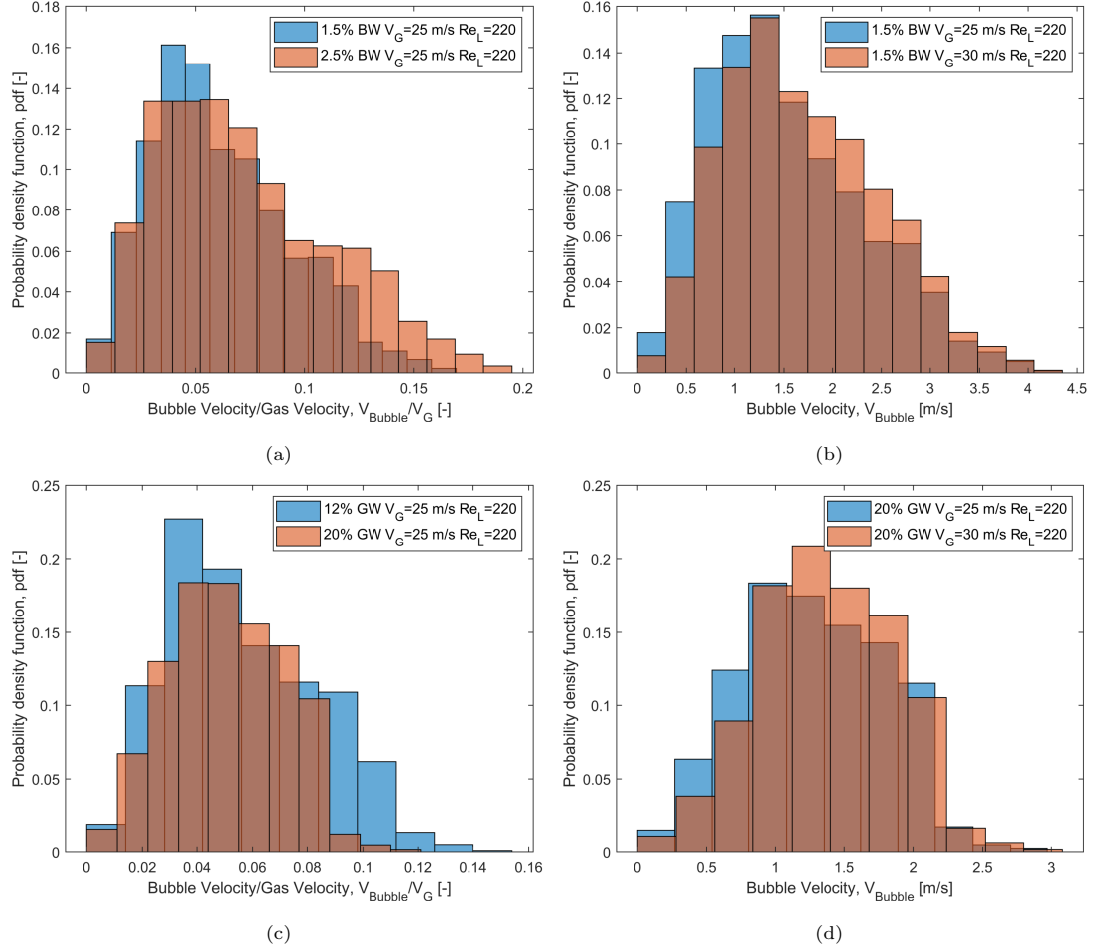


Figure 17: Comparison of bubble velocity probability density function between (a) two B-W concentrations at $V_G = 25$ m/s and $Re_L = 220$ (b) two gas velocities - $V_G = 25$ m/s and 30 m/s at 1.5% B-W, $Re_L = 220$ (c) two G-W concentrations at $V_G = 25$ m/s and $Re_L = 220$ (d) two gas velocities - $V_G = 25$ m/s and 30 m/s at 12% GW, $Re_L = 220$.

impact of these droplets has been shown previously to be one of the major causes of bubble generation in annular sheared flow [7]. A large number of bubbles entrapped in the fluid can cause foaming which is undesirable if the fluid is to be pumped and would also affect the heat transfer if the fluid is used for cooling applications.

While the focus of this paper is on the aeration in the flow, it is important to note the presence of bubbles and misting can affect the heat transfer between the gas, the liquid and the wall. Since decrease of the surface tension increases the mist density, this will correlate to an increase in the mass and heat transfer between the liquid and the gas. An increase in the viscosity does not significantly increase the number of droplets shed from the waves and can in fact decrease misting if the flow jumps to a different regime as shown in Figure 3. When these droplets impact on the surface of the liquid to generate the bubbles, this enhances the mass and heat transfer from the gas to the liquid. Where there are many bubbles there is a lot of surface area for heat transfer from the gas to the liquid. The results here show that decreasing the surface tension is the most efficient way of increasing mass and heat transfer between the gas and liquid phases in sheared flow configurations.

The increase in bubbles in such a thin film can inhibit the heat transfer between the wall and the liquid. The bubbles can act as an insulator between the the fluid trapped close to the wall and the surface of the film. Increasing the viscosity appears to make the bubbles more resilient to the turbulence in the liquid flow; hence increasing aeration. This will also affect the heat transfer between the liquid and the wall.

Also important is the role of the speed of the gas on this phenomenon. As the gas speed increases, the film thickness will reduce, the number of droplets will increase, which increases the number of bubbles trapped in the fluid. It is not shown here, but decreasing the surface tension may change the transition velocity for the onset of misting. As stated earlier, increasing viscosity can decrease misting since the flow changes to a smoother regime as Re_L decreases and Re_L decreases as viscosity increases for the same liquid loading factor.

7. Conclusion

This work is focussed on understanding the misting and foaming phenomenon due to the interaction between the liquid and the gas in two-phase sheared applications. This understanding could potentially lead to more efficient sub-system which could allow engineers to build more environmentally friendly systems. To help with our understanding, in the work in this paper we varied the liquid surface tension and viscosity and investigated its effect on bubble generation and film statistics in gas-sheared flows. The liquid properties were changed by adding butanol and glycerol to water, altering the surface tension from water's value of $72 \text{ mN}\cdot\text{m}^{-1}$ to $40 \text{ mN}\cdot\text{m}^{-1}$, and the dynamic viscosity from water's value of 1 cP to 1.9 cP . The gas velocities and liquid Reynolds number were chosen so that we are mostly in the misting regime and produced the following conclusions:

- From the film statistics, it was concluded that the film thickness is affected by the change in both liquid surface tension and viscosity. For both cases, the film thickness increases as compared to water due to aeration. From the measurement of base film thickness, it can be concluded that the gas velocity has more influence on the film thickness as compared to the liquid Reynolds number. However, the disturbance wave velocity was found to be higher for the water cases as compared to G-W and B-W cases. This is in-line with the mass balance of the liquid phase. Moreover, it can also be concluded that reducing the surface tension will shift the flow towards the disturbance waves regime, whilst higher viscosity dampens this transition and the flow will transit towards a less wavy regime.
- The frequency of the disturbance waves increases for the B-W cases as compared to G-W and water cases. However, the spacing of the disturbance waves was found to decrease with reduction in surface tension. This shows that the film surface is covered with a large number of wavy structures. Both the amplitude and longitudinal size of disturbance waves was found to decrease with gas velocity and and increase with liquid flow rate. However, no significant difference in wave amplitude and size was observed when the liquid properties were changed as compared to water.

- In this paper, we show that a decrease in surface tension will increase the aeration in the flow. We also show that increasing liquid viscosity leads to higher aeration in the flow but not to the same extent as reduction in surface tension does. A comparison to Rodrigues and Shedd [8] and Hann et al. [7] shows that the bubble size distribution exhibits exponential decay. Contrary to [8] it is shown that the exponential decay for the different cases has closer similarity when the bubble size is not normalized by the mean film thickness. The exponential constant of the bubble size distribution was found to decrease with liquid Reynolds number. The bubble size distribution for the B-W cases was found to be similar at higher V_G and Re_L . This observation was also confirmed from the quantile-quantile plots.
- As expected from Hann et al. [7] larger bubbles were found to be present in the disturbance waves. These bubbles are formed in the base film and get entrained in the disturbance wave. When we increase the viscosity, the bubble velocity decreases; however, when the surface tension is decreased, the bubble velocity was found to increase.

These results have shown that this a very complicated situation and that further work be done to understand the complex heat and mass transfer that happens in this relatively simple configuration if we want to understand more complex situation.

8. Acknowledgements

The authors would like to thank Rolls-Royce plc and Innovate UK for their support of the COAST project, which provided the research rig and supported the data analysis. The study of the wave structure was supported by Russian Science Foundation (project 19-19-00287). The analysis of the entrapped bubbles was progressed via COAST.

References

- [1] A. Cherdantsev, J. An, A. Charogiannis, C. Markides, Simultaneous application of two laser-induced fluorescence approaches for film thickness measurements in annular gas-liquid flows, *International Journal of Multiphase Flow* 119 (2019) 237–258.
- [2] M. Holowach, L. Hochreiter, F. Cheung, A model for droplet entrainment in heated annular flow, *International journal of heat and fluid flow* 23 (6) (2002) 807–822.
- [3] R. Oliemans, et al., Multiphase science and technology for oil/gas production and transport, in: *University of Tulsa Centennial Petroleum Engineering Symposium*, Society of Petroleum Engineers, 1994.
- [4] J. Vasques, A. Ibrahim, D. Hann, K. Simmons, M. Walsh, The effect of surface tension on bubble generation in gas-sheared liquid films, in: *Turbo Expo: Power for Land, Sea, and Air*, Vol. 58646, American Society of Mechanical Engineers, 2019, p. V05AT13A008.

- [5] N. H. Taylor, G. Hewitt, The motion and frequency of large disturbance waves in annular two-phase flow of air-water mixtures, *Chemical Engineering Science* 18 (8) (1963) 537–552.
- [6] A. V. Cherdantsev, D. B. Hann, B. N. Hewakandamby, B. J. Azzopardi, Study of the impacts of droplets deposited from the gas core onto a gas-sheared liquid film, *International Journal of Multiphase Flow* 88 (2017) 69–86.
- [7] D. B. Hann, A. V. Cherdantsev, B. J. Azzopardi, Study of bubbles entrapped into a gas-sheared liquid film, *International Journal of Multiphase Flow* 108 (2018) 181–201.
- [8] D. J. Rodriguez, T. A. Shedd, Entrainment of gas in the liquid film of horizontal, annular, two-phase flow, *International journal of multiphase flow* 30 (6) (2004) 565–583.
- [9] R. Mesler, A mechanism supported by extensive experimental evidence to explain high heat fluxes observed during nucleate boiling, *AIChE Journal* 22 (2) (1976) 246–252.
- [10] J. Barbosa Jr, G. Hewitt, S. Richardson, High-speed visualisation of nucleate boiling in vertical annular flow, *International journal of heat and mass transfer* 46 (26) (2003) 5153–5160.
- [11] I. Zadrazil, C. N. Markides, An experimental characterization of liquid films in downwards co-current gas–liquid annular flow by particle image and tracking velocimetry, *International Journal of Multiphase Flow* 67 (2014) 42–53.
- [12] M. Sadatomi, A. Kawahara, M. Matsuo, K. Ishimura, Effects of surface tension on two-phase gas-liquid flows in horizontal small diameter pipes, *Journal of Power and Energy Systems* 4 (2) (2010) 290–300.
- [13] Y. Rivera, J.-L. Muñoz-Cobo, J.-L. Cuadros, C. Berna, A. Escrivá, Experimental study of the effects produced by the changes of the liquid and gas superficial velocities and the surface tension on the interfacial waves and the film thickness in annular concurrent upward vertical flows, *Experimental Thermal and Fluid Science* (2020) 110224.
- [14] T. Fukano, T. Furukawa, Prediction of the effects of liquid viscosity on interfacial shear stress and frictional pressure drop in vertical upward gas–liquid annular flow, *International journal of multiphase flow* 24 (4) (1998) 587–603.
- [15] Y. Yoshinaga, C. Dang, E. Hihara, Experimental study on two-phase flow pattern and liquid film thickness of slug flow in horizontal microchannels, *Trans. of the JSRAE* 31 (2) (2014) 9–22.
- [16] S. Alekseenko, A. Cherdantsev, D. M. Markovich, A. Rabusov, Investigation of droplets entrainment and deposition in annular flow using lif technique, *Atomization and Sprays* 24 (3).
- [17] S. V. Alekseenko, A. V. Cherdantsev, O. M. Heinz, S. M. Kharlamov, D. M. Markovich, Analysis of spatial and temporal evolution of disturbance waves and ripples in annular gas–liquid flow, *International journal of multiphase flow* 67 (2014) 122–134.

- [18] S. Alekseenko, V. Antipin, A. Cherdantsev, S. Kharlamov, D. Markovich, Investigation of waves interaction in annular gas-liquid flow using high-speed fluorescent visualization technique, *Microgravity Science and Technology* 20 (3-4) (2008) 271–275.
- [19] J. Vasques, A. Cherdantsev, M. Cherdantsev, S. Isaenkov, D. Hann, Comparison of disturbance wave parameters with flow orientation in vertical annular gas-liquid flows in a small pipe, *Experimental Thermal and Fluid Science* 97 (2018) 484–501.
- [20] W. Fan, A. V. Cherdantsev, H. Anglart, Experimental and numerical study of formation and development of disturbance waves in annular gas-liquid flow, *Energy* 207 (2020) 118309.
- [21] K. Pancholi, E. Stride, M. Edirisinghe, Dynamics of bubble formation in highly viscous liquids, *Langmuir* 24 (8) (2008) 4388–4393.